A Wide-field Imaging Approach for Simultaneous Super-Resolution Surface-Enhanced Raman Scattering Bioimaging and Spectroscopy

Deben N. Shoup,[1] Brian T. Scarpitti,[1] and Zachary D. Schultz[1,2,*]

1. Department of Chemistry and Biochemistry, The Ohio State University, Columbus, Ohio 43210, USA

2. Comprehensive Cancer Center, The Ohio State University, Columbus, Ohio 43210, USA

* corresponding author email: schultz.133@osu.edu

Abstract

High spatial resolution imaging and chemical specific detection in living organisms is important in a wide range of fields, from medicine to catalysis. In this work, we characterize a wide-field surface enhanced Raman scattering (SERS) imaging approach capable of simultaneously capturing images and SERS spectra from nanoparticle SERS-tags in cancer cells. By passing the image through a transmission diffraction grating before it reaches an array detector, we record the image and wavelength dispersed signal simultaneously on the camera sensor. Optimization of the experiment provides an approach with better spectral resolution and more rapid acquisition than liquid crystal tunable filters commonly used for wide-field SERS imaging. Intensity fluctuations inherent to SERS enabled localization algorithms to be applied to both the spatial and spectral domain, providing super-resolution SERS images that are correlated with improved peak positions identified in the spectrum of the SERS tag. The detected Raman signal is shown to be sensitive to the focal plane, providing 3D sectioning abilities for the detected nanoparticles. Our work demonstrates spectrally resolved super-resolution SERS imaging that has potential to be applied to complex physical and biological imaging applications.

Keywords

SERS, super-resolution, microscopy, Raman, bioimaging, spectroscopy

Introduction

The ability to image molecules on dimensions relevant to chemical interactions has tremendous potential to advance understanding for diverse applications from medicine and pharmaceuticals, to the environment, advanced materials and sensors.[1-4] The non-invasive nature of optical microscopy can monitor systems under living (*in vitro* or *in vivo*) as well as under operating (*in operando*) conditions. Advances in optical imaging, enabling single molecule localization,[5-10] have enabled unprecedented visualization of these dynamic processes. Equally important to locating the molecules is the ability to detect chemical changes and interactions occurring.

Vibrational spectroscopy has been used to monitor these chemical processes by detecting the energy associated with chemical bonds to identify and quantify species.[11, 12] Infrared and Raman imaging have both advanced to enable label-free detection based on the chemical properties of the samples. The spatial resolution of these vibrational techniques is typically limited by the diffraction limit ($d = \lambda/2\,NA$), where the spot diameter (d) is a function of the wavelength (λ) and the numerical aperture of the lens (NA) while the spectral resolution and acquisition speed are often determined by the cross section of the sample. Raman has an intrinsic advantage in spatial resolution associated with shorter wavelengths of visible lasers relative to infrared radiation; however, the small cross sections typical of most Raman processes lead to long acquisition times. A number of different approaches (e.g., point scanning, line scanning, multipoint scanning, wide-field imaging, etc.) have been demonstrated to image and resolve the energy differences present in chemical samples.[11, 13-16] In addition to linear or spontaneous spectroscopies, nonlinear approaches have also been investigated to increase the speed and sensitivity of vibrational imaging.[17-19]

The enhancement of Raman signals on plasmonic nanoparticles, surface enhanced Raman scattering (SERS), provides dramatic signal increases that enable new opportunities for Raman measurements.[20-23] The electric fields confined to the surface of the nanoparticles generate an intense molecular signal that transforms Raman into an ultrasensitive, even single molecule, detection method.[24, 25] This has led to the development of SERS tags that can be functionalized with antibodies, nucleotides, or other affinity agents providing a unique signal for detection.[26-28] The interaction of other molecules with the nanoparticles can also increase the observed Raman signal, providing increased sensitivity for label free detection.[29] The signals observed in SERS

have been shown to be transient and the magnitude of transient SERS fluctuations is often missed if the signal is averaged over extended acquisition times.[30, 31] Additional rapid intensity fluctuations, SERS intensity fluctuations (SIFs), are also observed arising from dynamic events on individual nanoparticles.[32] These intense SERS responses can be recorded on time scales limited by the detectors.

The intense signals associated with SERS have given rise to super-resolution SERS imaging.[33] The intense SERS signals can be fit with localization algorithms, such as those used in stochastic optical reconstruction microscopy (STORM),[34] to generate images corresponding to location of single molecule emitters.[35] Super-resolution SERS has been used to map hot-spots in nanoparticle dimers,[36] SIFs on microsecond time scales,[37] hotspots in plasmonic arrays,[38] and protein receptors in cultured cancer cells.[39] These approaches commonly bin the Stokes scattering to produce a larger signal detectable on array detectors. The ability to correlate the SERS spectrum with the emitter has also been demonstrated. One report showed a liquid crystal tunable filter (LCTF) preserved the chemical information in wide field SERS imaging.[40] LCTFs can provide a narrow spectral bandpass (typically 10 nm); however, the throughput is low. An alternate approach for spectral imaging is snapshot imaging, where the image is passed through a transmission diffraction grating in close proximity to the array detector.[38, 41-43] The sensor simultaneously captures the image and the first order diffraction, the latter corresponding to the spectrum. This approach has been used by others to resolve SERS from array substrates,[38] fluorescence,[41, 43] and the electronic scattering spectrum from nanoparticles.[42] In our prior work,[44] we demonstrated the SERS intensity fluctuations on asymmetric nanoparticles correlated with chemical transformations. We were able to correlate SERS spectra with 10-100 ms temporal fluctuations to the location of the emissions on the nanoparticle with sub-diffraction limited resolution.

The ability to super-resolve the location and measure the SERS spectrum simultaneously suggests new opportunities for SERS imaging. Tip-enhanced Raman spectroscopy (TERS) has provided sub-nm spatial resolution imaging, but requires access to the molecules by a scanning probe microscope tip.[45, 46] The ability to super-resolve and simultaneously record the spectrum, by the snapshot imaging approach noted above, of a molecule on a nanoparticle suggests the possibility of nano-spectroscopy from molecules buried within complex samples. In the present work, we explore the instrumentation and performance of super-resolution SERS spectral imaging

of silica shell, mercaptobenzoic acid (MBA) functionalized, gold nanoparticles (AuNP@Silica) and the ability to locate the nanoparticles and measure the spectrum in cancer cells. Optimization of the signal collection provides wide field imaging with spectral resolution better than an LCTF that also records the full spectrum in each acquisition. Recording the full spectrum in each frame enables monitoring of chemical interactions in the imaged sample. The MBA molecules detected here provide a distinct SERS spectrum that can be used to validate the particles detected and associated chemical processes. Fluctuations in the SERS intensity are processed to super-resolve the location of the nanoparticles using existing algorithms. In our results, we also evaluate the use of intensity fluctuations in the spectral response to provide improved precision of peak position in the measured spectra. Optimization and characterization of the instrumentation shows how the size of the imaged object impacts spectral resolution. The intensity of the SERS signal is shown to vary dramatically with the focal plane, providing 3D imaging capability. Our results demonstrate simultaneous detection of both the image and SERS spectrum of nanoparticles in cells and open new possibilities for monitoring chemical processes in complex systems.

Methods

Synthesis and Characterization of AuNP@Silica nanoparticles

Spherical gold nanoparticles were made by reduction with citrate as reported previously[47] to produce a suspension of $5.7(\pm0.5)x10^{10}$ nanoparticles mL^{-1}. The average size of the nanoparticles was determined by dynamic light scattering to be 40 nm. To 10 mL of the nanoparticle suspension, 100 μL of 40 mM MBA was added; the solution shook for 30 minutes, was pelleted, and was resuspended in water using 20% of the original volume. The gold nanoparticles were encapsulated in silica by adding 6 mL EtOH and 0.4 mL NH_4OH per 2 mL particles and then immediately adding the solution into 20 mL IPA, 20 μL TEOS, and 0.3 mL water per 2 mL particles. This solution shook for 19 hours. The resulting suspension was pelleted by centrifugation in 4x 10 mL tubes (30 min x 3000 g), and each pellet was washed twice in 1 mL 1:1 EtOH: water by resuspending in this solution and pelleting by centrifugation for 20 min at 3000 g. This suspension was then centrifuged again (20 min x 3000 g) and resuspended in 2 mL water total.

Ensemble SERS spectra of the AuNP@Silica particles were obtained with a Snowy Range Instruments IM-52 Raman spectrometer. A 638 nm laser using 23 mW power and 10 s acquisition

time were used. Extinction spectra were obtained with a VWR UV-1600 PC spectrometer. A Tecnai 30 transmission electron microscope (TEM) was used for electron microscopy. Prior to spectrally resolved SERS imaging, the nanoparticles were dropped onto a glass coverslip.

Cell Culturing and Fixation

Human SW620 colon cancer cells derived from commercial cell lines (ATCC, Manassas, VA, USA) were passaged at approximately 80% confluency in RPMI-1640 medium supplemented with 10% FBS. The cells were cultured in a humidified atmosphere containing 5% CO_2 with a temperature of 37 °C in accordance with previously published protocols.[48]

Glass coverslips were cleaned in Alnochromix™ solution and autoclaved. Cells were added to coverslips two days prior to the addition of nanoparticles. Twenty-four hours after particles were added to the cells, the cells were fixed by removing the media from the cells, adding paraformaldehyde (4% in PBS) to the cells for 15 minutes, and rinsing with PBS. The paraformaldehyde was then removed, and the cells were rinsed with 6 mL PBS followed by 3 mL water.

Spectrally Resolved SERS Imaging

The samples were illuminated using a 659 nm single longitudinal mode diode laser (Laser Quantum) with a variable power output from 0-300 mW. The laser was directed onto the samples through a f=75 mm plano-convex lens (Thorlabs). An inverted microscope (IX-71, Olympus) with a 100x, 1.3 NA oil immersion objective (Olympus) was used for imaging. The scattered light was collected and passed through a 638 nm long pass dichroic mirror (Thorlabs) and a 660 nm long pass edge filter (Semrock) before exiting the microscope. The collected light was then directed through a 300 groove/mm visible transmission diffraction grating with a 17.5° blaze angle (Thorlabs) and onto a 2-dimensional scientific complementary metal-oxide-semiconductor (sCMOS, ORCA-Flash 4.0 V2, Hamamatsu, LTD). The sCMOS sensor used is a 2048 x 2048 array with 6.5 μm pixels.

Calibration

For calibration experiments, a 20x 0.45 NA, 40x 0.60 NA, or 100x 0.8 NA (Olympus) objective was used. The 659 nm laser or a 6032 Ne calibration lamp (Newport) was directed through a 1 or 5 μm pinhole (Thorlabs) and imaged on the sCMOS camera. To correlate wavelength and pixel location from the n=0 order, the pixels in the y-direction containing the signal (4-20 rows depending on the size of the pinhole and objective used) were averaged together

and the average intensity profile was plotted. Known Ne emission wavelengths were plotted against the distances between the most intense pixel from the 0^{th} order and each of the peaks in the 1^{st} order to create a calibration curve. The slope of the calibration curve is the observed dispersion and was used to calculate the wavelength at each pixel from the most intense pixel in the 0^{th} order image. The wavelength at each pixel was subsequently converted to Raman shift for SERS experiments.

Data Processing and Analysis

Images were acquired using the NIS-Elements Advanced Research software (Nikon) at a 5 Hz frame rate for 1000 frames and a 1 Hz frame rate for 20 frames for AuNP@Silica particles on a glass surface and on fixed cells, respectively. ImageJ (U.S. National Institutes of Health) was used for image analysis and Matlab (Mathworks) was used for spectral analysis. To generate intensity profiles and spectra, the rows of pixels containing the signal in the y-direction were averaged together depending on the size of the particle or pinhole. A range of 5-8 and 4-20 rows of pixels were averaged together for AuNP@Silica particles and pinholes, respectively. The ThunderSTORM plug in for ImageJ was used for STORM fittings and analysis.[49]

Results

Spectrally Resolved SERS Imaging

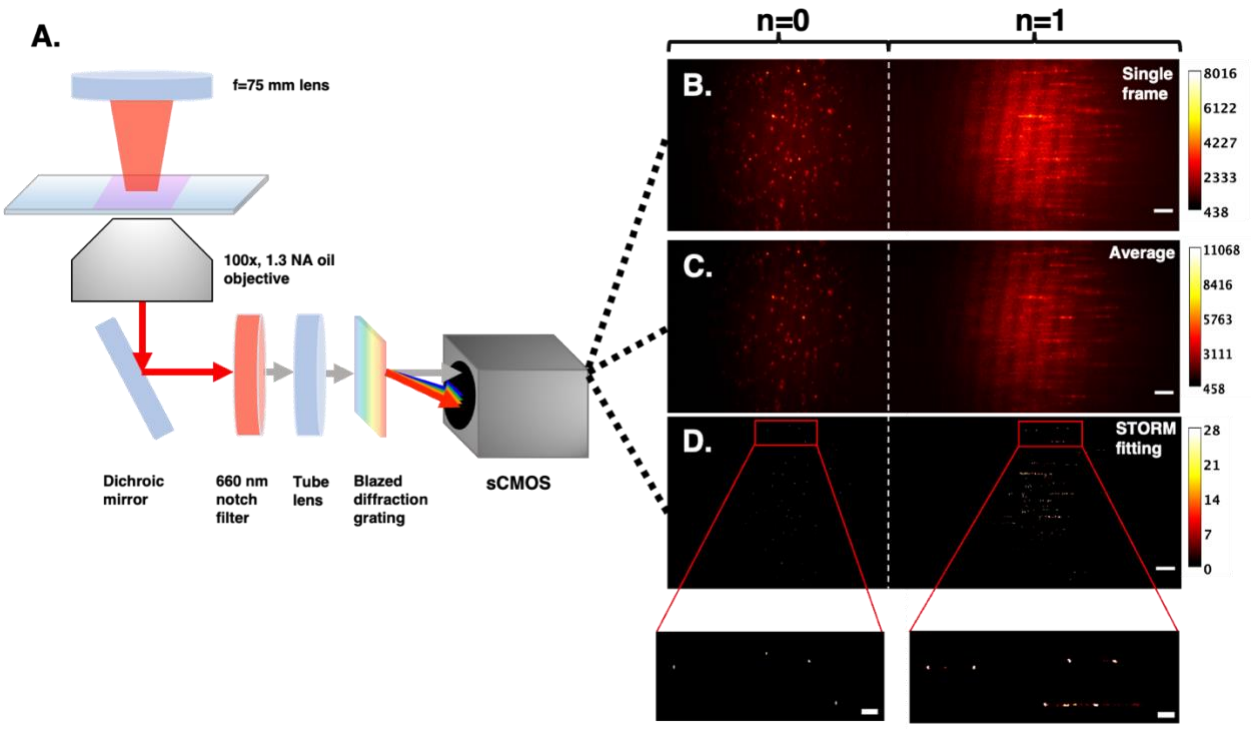

Figure 1. Illustration of spectrally resolved SERS imaging measurement. A) A homebuilt spectrally resolved SERS imaging instrument is built around an Olympus IX-71 inverted microscope. The light from wide-field illumination with a 659 nm laser is collected by the microscope, filtered through a 660 nm longpass filter, and then the image is dispersed with a transmission diffraction grating immediately before the sCMOS sensor. B) A single frame of the signal detected on the CMOS array is shown. C) The average of 1000 consecutive frames collected at 5 Hz is shown. D) The ThunderSTORM localization image is generated from analysis of the image stack in (C). The sample used in B-D is AuNP@Silica particles. The scale bars in B-D are 5 µm. The blown-up regions are provided to help visualize the features in (D). The scale bar for the inset is 1 µm.

Figure 1A illustrates our homebuilt spectrally resolved SERS imaging experiment. Briefly, the 659 nm excitation laser passes through a convex lens positioned at its focal length above the sample. This enables a wide-field field of view (FOV) by focusing the laser to a spot illuminating an area of 35 µm in diameter (Figure S1) resulting in a power density of 7.3 kW cm^{-2} at the sample. The scattered light is collected with a 100x, 1.3 NA oil objective, and the Raman scattered signal passes through a 638 nm dichroic mirror and a 660 nm notch filter prior to exiting the microscope. The dichroic mirror and notch filter attenuates the anti-Stokes and Rayleigh scattering so that the Stokes scattered Raman light is prevalent in the detected image. The position of the filters before the tube lens is important to avoid a spectral offset in the detected image associated with passing

convergent light through the filter. The collected light then passes through a blazed diffraction grating and the n=0 (spatial) and n=1 (spectral) order diffraction is imaged onto a sCMOS detector.

To demonstrate this technique, AuNP@Silica particles with a localized surface plasmon resonance (LSPR) of 548 nm (Figure S2) were imaged. TEM images of the AuNP@Silica particles are shown in Figure S3. Figure 1B and 1C show the n=0 and n=1 FOV for a single frame and the average of 1000 frames, respectively. SIFs are a common occurrence with single molecule SERS but also with single particles functionalized with a monolayer.[32, 37, 50] SIFs and temporal fluctuations associated with Raman scattering enable super resolution/localization algorithms such as STORM to be applied by fitting the point spread function (PSF) of the nanoparticle signal fluctuations to a 2D-Gaussian.[39, 51, 52] By plotting the center of the PSF for each emitter, the position of the emitting center of the nanoparticle is localized to a few pixels. For particles with near uniform coverage of the molecule, the emission is weighted average of all emitters on the particle.[53] As previously described, the first order diffraction (n=1) provides the Raman spectrum associated with the spectral intensity in the n=0 image.[44] Because the intensity of the n=1 order fluctuates simultaneously with the n=0 order, STORM algorithms can also be applied to the spectral region. Figure 1D shows the STORM fitting output generated from the image stack. The particles detected in Figure 1D have an average FWHM of 70 nm, which is below the diffraction limited resolution of 254 nm.

Careful consideration of several factors that impact the performance of the instrument was taken, namely the distance between the grating and the sCMOS sensor, which dictates the dispersion in the n=1 order, and the illumination spot size. In order to use as much as the detector as possible without overlapping features, these parameters were chosen such that the n=0 order and n=1 order fill about 1/3 and 2/3 of the detector in the x-direction, respectively (Figure 1).

Optimization of Instrument Performance

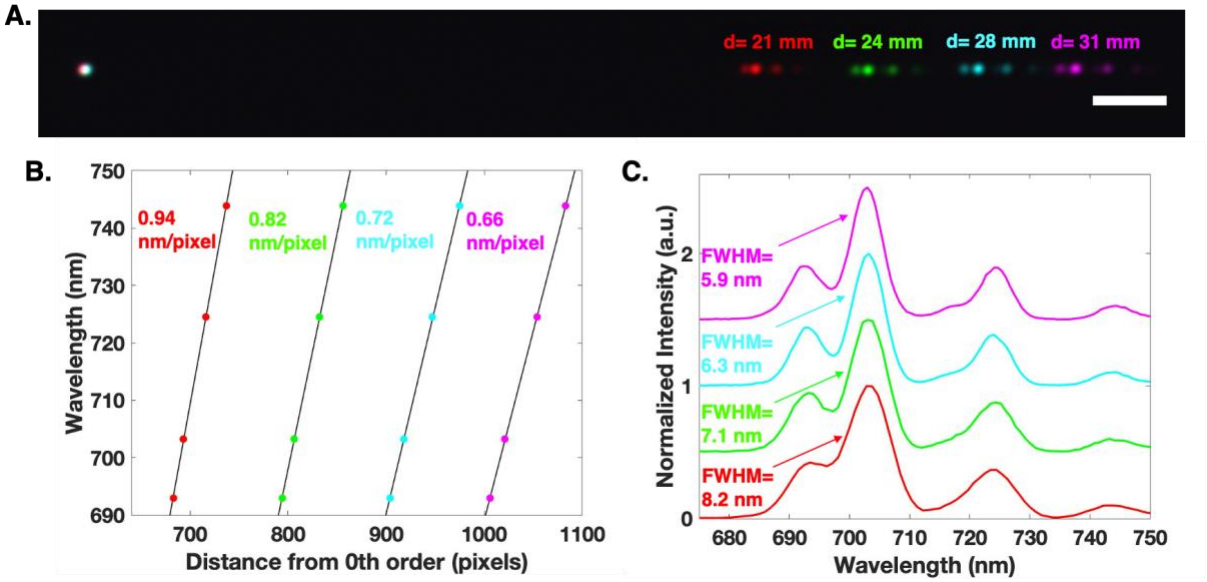

Figure 2. The dispersion detected in n=1 is shown as a function of distance from grating to sCMOS detector from a Ne calibration lamp through a 1 µm pinhole. A) The overlay of 0th order (left) and 1st order (right) diffraction images collected at varying distances between the grating and CMOS sensor. B) A plot of wavelength vs number of pixels from the 0th order feature produces calibration curves showing the expected increase in dispersion as the distance between the grating and sensor increases. The sensor has been cropped to the region of interest. C) Calibrated spectra from the 1 µm pinhole illuminated with a neon lamp and imaged at diffraction grating to sensor distances of 21 mm (red), 24 mm (green), 28 mm (cyan), 31 mm (pink) show the expected changes in the FWHM for the detected Ne emission lines. The spectra in (C) are normalized and offset for clarity.The scale bar in (A) is 5 µm. The black lines in (B) are linear best fit lines.

Dispersion and the size of the source image were analyzed in an effort to determine and maximize spectral resolution of our imaging system. To experimentally determine dispersion in the n=1 order, we moved the sCMOS sensor to vary the distance between the sensor and diffraction grating and illuminated a 1 µm pinhole with a Ne calibration lamp. Figure 2A shows an overlay of the raw images taken over a 10 mm distance increase with an improvement in the dispersion as the distance increases. The intensity profiles of the n=1 responses were plotted with respect to number of pixels from the n=0 order for each grating-to-detector distance and then used to make calibration curves for each distance (Figure 2B). The observed dispersion was determined from the slope of the calibration lines and reported in Figure 2B. The observed dispersions are in good agreement with the calculated dispersions (Table S1), especially as the dispersion improves. From there, the wavelength at each pixel from the n=0 order was calculated, and the intensity profiles

were plotted with respect to wavelength (Figure 2C). Because the wavelength is calibrated at each pixel from the most intense pixel in the n=0 portion of the sensor, calibrated spectra can be readily plotted by correlating the n=1 signal to the n=0 pixel containing the most intense signal in the collected image.

Figure 2C shows the improvement in spectral resolution as the distance between grating and detector increases while the size of the pinhole in the n=0 order is constant. The full width at half maximum (FWHM) for the most intense (703.2 nm) peak was calculated and shows a 2 nm improvement with a 10 mm distance increase. For the remainder of the experiments, the distance between the grating and sensor was kept constant at 31 mm with a dispersion of 0.66 nm/pixel. This distance was chosen not only for the dispersion improvement, but this prevents overlap between the n=0 and n=1 order and the n=1 dispersions for each nanoparticle illuminated in the n=0 order image onto the detector using a 35 μm illuminated FOV on the sample.

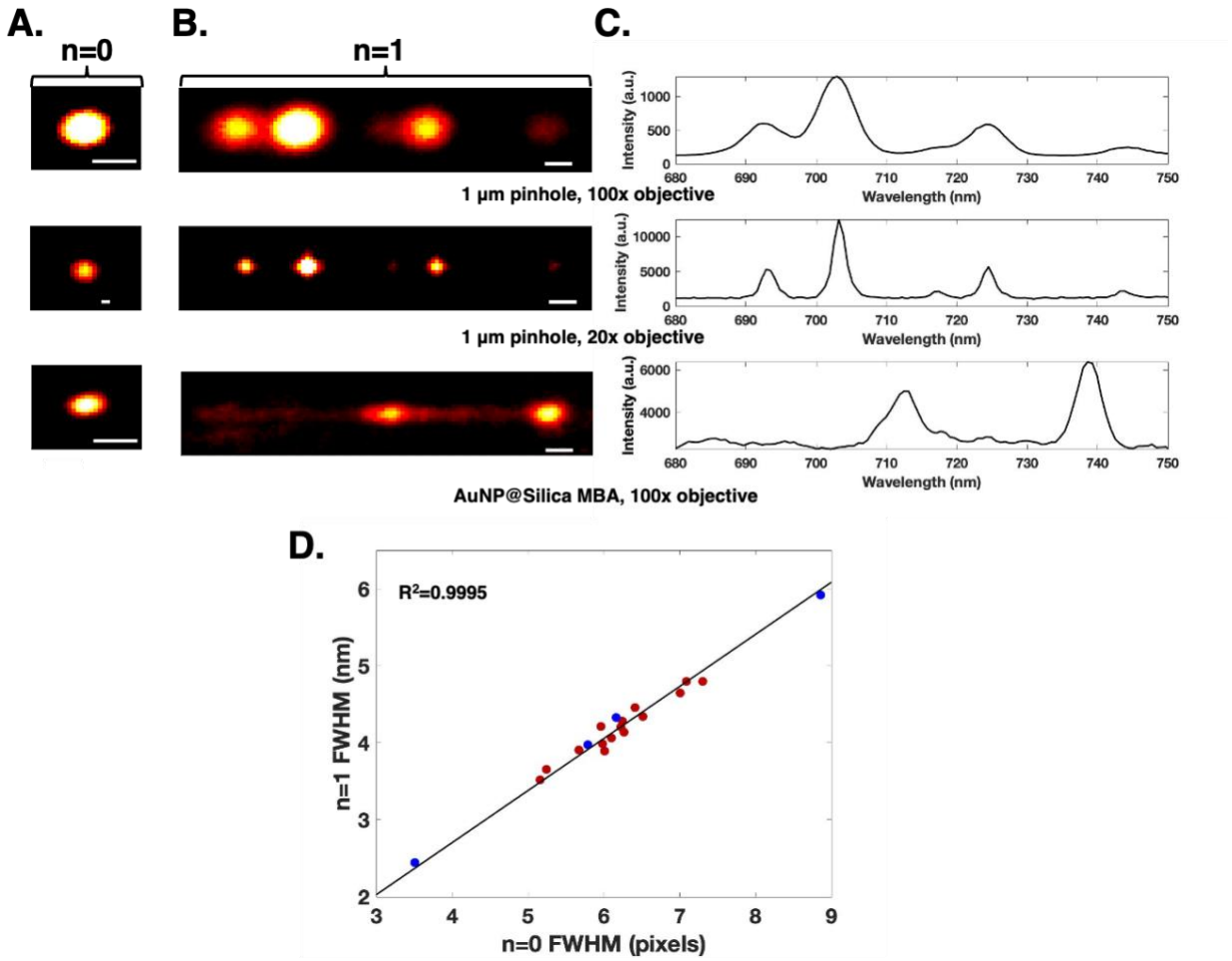

Figure 3. Images of the (A) n=0 and (B) n=1 orders and (C) spectra from the n=1 order images of a 1 µm pinhole illuminated with a Ne lamp and imaged with a 100x (top) and 20x objective (center) and a AuNP@Silica particle imaged with a 100x objective (bottom). The region of interest on the sensor has been cropped to highlight the detected signals. Scale bars are 650 nm in the n=0 domain and 5 nm in the n=1 domain. D) Plot of FWHM of the n=1 domain with respect to FWHM of the n=0 domain for 15 AuNP@Silica particles and 1 µm pinhole illuminated with a Ne lamp and imaged with a 20x, 40x, and 100x objective and a 5 µm pinhole illuminated with a Ne lamp imaged with a 20x objective. The pinholes and AuNP@Silica particles are indicated by the blue and red markers, respectively. The most intense band was used to determine FWHM in the n=1 order. A linear trendline is indicated by the black line.

In addition to the dispersion, the spectral resolution is limited by the number of pixels in the n=0 order image, or the size of the source image. The textbook relationship: $\Delta\lambda = w\, D^{-1}$, indicates the resolution ($\Delta\lambda$), or wavelength uncertainty, is limited by the linear reciprocal dispersion (D^{-1}) and the slit width (w). Classically, the wavelength uncertainty in a spectrum is

limited by the spectrometer slit width. However, in our approach, the observed size of the emitter image acts as a virtual slit that, in combination with the dispersion, controls the spectral resolution. To demonstrate this, we illuminated a 1 μm pinhole with a Ne lamp and imaged with a 100x and 20x objective and compared the spectral resolution of the pinhole to a AuNP@Silica particle from Figure 1. Imaging the pinhole with various magnification objectives effectively changes the size of the virtual slit, which changes the observed spectral resolution. The images of the n=0 and n=1 domains of the pinhole and nanoparticle are shown in Figure 3A and B, respectively. The spectra from those images are shown in Figure 3C. To demonstrate how the spectral resolution changes across a range of image sizes, 1 and 5 μm pinholes imaged with various magnification objectives and AuNP@Silica nanoparticles were analyzed. The emitter image sizes were estimated by plotting the intensity profiles of the n=0 order images and finding the FWHM. Spectral resolution in the n=1 domain was estimated by plotting the intensity profiles from the images and finding the FWHM of the most intense bands (703 nm for Ne and 736 nm for MBA). Figure 3D shows a plot of the n=1 FWHM with respect to n=0 FWHM from 15 AuNP@Silica particles and 1 μm and 5 μm pinholes illuminated by a Ne lamp, showing a linear relationship between the size of the object in the n=0 order and spectral resolution in the n=1 order. The slope of the linear trendline is 0.68 nm/pixel, which is in good agreement with the expected dispersion (Table S1). The emission lines from the Ne calibration lamp are expected to be limited by the resolution of the measurement. The width of the Raman lines detected are expected to be broader and may show spectral shifts associated with plasmonic effects.[54-57]

Spectrally Resolved SERS imaging of AuNP@Silica

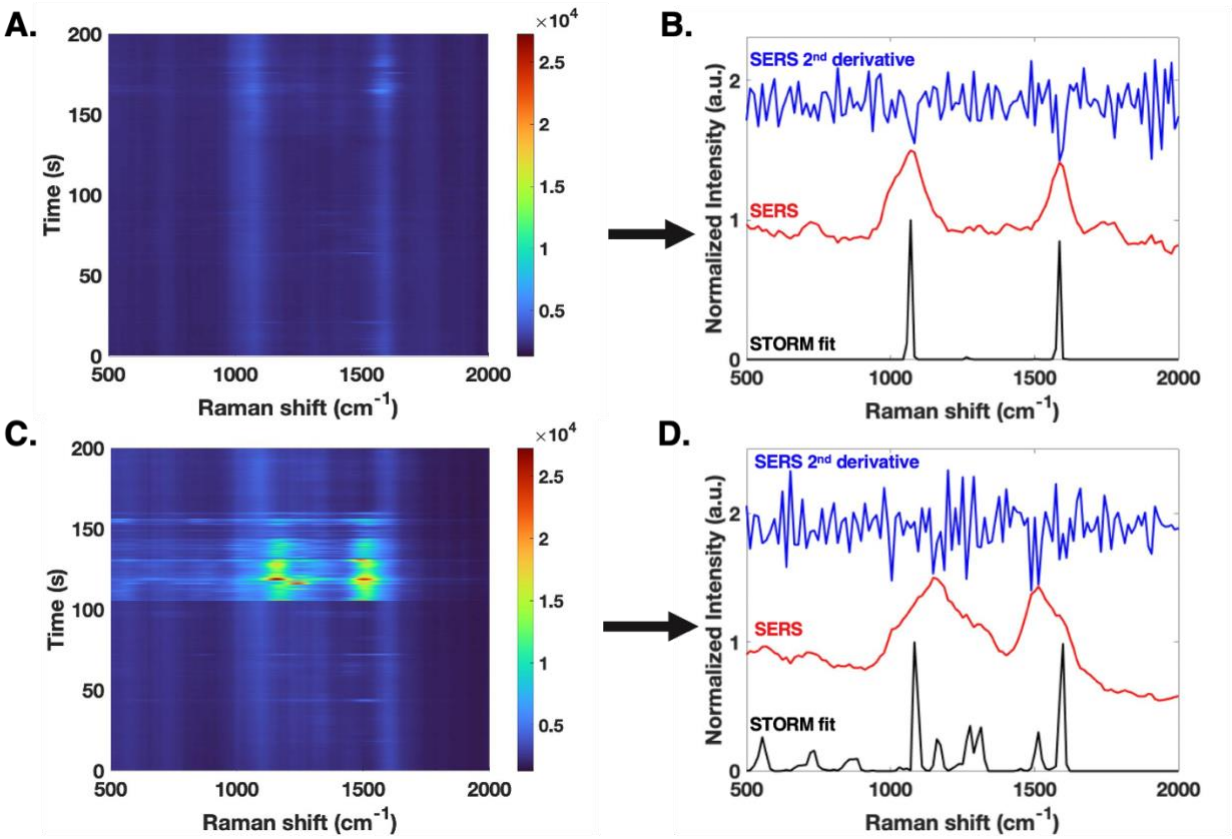

Figure 4. Time resolved spectroscopy of imaged AuNP@Silica particles. A) Temporal fluctuations in the SERS spectra are observed. B) The average spectrum (red), 2nd derivative spectrum (blue), and the result of STORM analysis on the fluctuation in the spectra (black) are shown from of a AuNP@Silica particle from Figure 1C that shows no frequency fluctuations during the acquisition. C) Time-varying frequency fluctuations in the SERS spectra and the corresponding (D) average spectrum (red), 2nd derivative spectrum (blue), and ThunderSTORM fitted spectrum (black) of a AuNP@Silica particle from Figure 1C that experiences frequency fluctuations during the acquisition. The spectra in (B) and (D) are normalized and offset for clarity. Both time varying SERS plots consist of 5 Hz acquisitions for 1000 frames.

Figure 4 shows the spectral response from two nanoparticles shown in Figure 1. Heat maps of SERS intensity from consecutive measurements over time for the two nanoparticles are shown in Figure 4A and C. The SERS response from the nanoparticle in Figure 4A shows two consistent bands throughout the signal collection centered at 1070 cm^{-1} and 1586 cm^{-1}, which are consistent with MBA SERS bands in the ensemble solution spectrum (Figure S4) attributed to aromatic ring vibrations.[58] Some intensity fluctuations occur, but the bands do not shift in energy as the measurement progresses. On the other hand, the SERS response from the nanoparticle in Figure

4C also has the 1070 cm^{-1} and 1586 cm^{-1} bands, but at ~100 s there are transient, intense peak shifts to 1250 cm^{-1} and 1480 cm^{-1}. Our group has shown with spectrally resolved SERS imaging that MBA adsorbed to gold nanostars may reveal the formation of radicals of MBA or photochemical reaction products.[44]

The red curves in Figure 4B and D show the ensemble averaged SERS spectrum from the 1000 frames used to generate the heat maps in Figure 4A and C, respectively. The average spectrum in Figure 4D shows two broad bands centered at 1148 cm^{-1} and 1513 cm^{-1} with the peak broadening and shifting attributed to the possible radical formation.[57] Applying STORM algorithms to the images localizes the emitting centers to a single or a few pixels in the n=0 order (Figure 1D), but also localizes the spectral fluctuations in the n=1 order. Plotting the STORM generated spectral responses results in significantly improved peak identification with the center of the peaks consistent with the raw SERS spectra. STORM results do not have an intensity-based scale like the SERS spectra, but rather produce a digital histogram based on the number of frames the emitter is fit to that pixel position.[49] The n=1 STORM fittings are plotted in black in Figure 4B and D. The STORM fit for the 1st nanoparticle has two peaks centered at 1070 cm^{-1} and 1586 cm^{-1}, the same positions as the average spectrum. Comparing this fit to the 2nd derivative spectrum (blue curve), the STORM fit provides a more distinct peak identification without having to apply smoothing or background correction, which would be needed to utilize the 2nd derivative spectrum to identify the peaks.

The localization algorithm applied to generate the super-resolved image can also be used to identify spectral fluctuations with improved precision. The n=1 STORM fitting for the 2nd nanoparticle (Figure 4D, black curve) also shows two distinct MBA peaks at 1083 cm^{-1} and 1599 cm^{-1} but it identifies the fluctuating components that are observed in the time-dependent spectra (Figure 4C) but are not cleanly resolved in the ensemble averaged spectrum (Figure 4D, red curve) or the 2nd derivative spectrum (Figure 4D, blue curve). The transient frequency fluctuations observed are more intense compared to the 1083 cm^{-1} and 1599 cm^{-1} bands and subsequently cause a shift in the average spectrum. The STORM analysis provides a peak fit to the fluctuating spectra and reports the peak centers observed in each frame. The Raman bands at 1083 and 1599 cm^{-1} are observed in more frames and thus have the highest count in the STORM spectral analysis. This is consistent with the STORM intensity scale being a digital expression of the peaks are present in the measurement. However, the ability to identify the centers of the frequency fluctuations

provides an improved method to correlate the frequency shifts to chemical phenomena. The combination of the peak positions from the STORM analysis with the intensity in the SERS signal enables improved spectral deconvolution.

Spectrally Resolved SERS Imaging of AuNP@Silica Particles in Fixed Cells

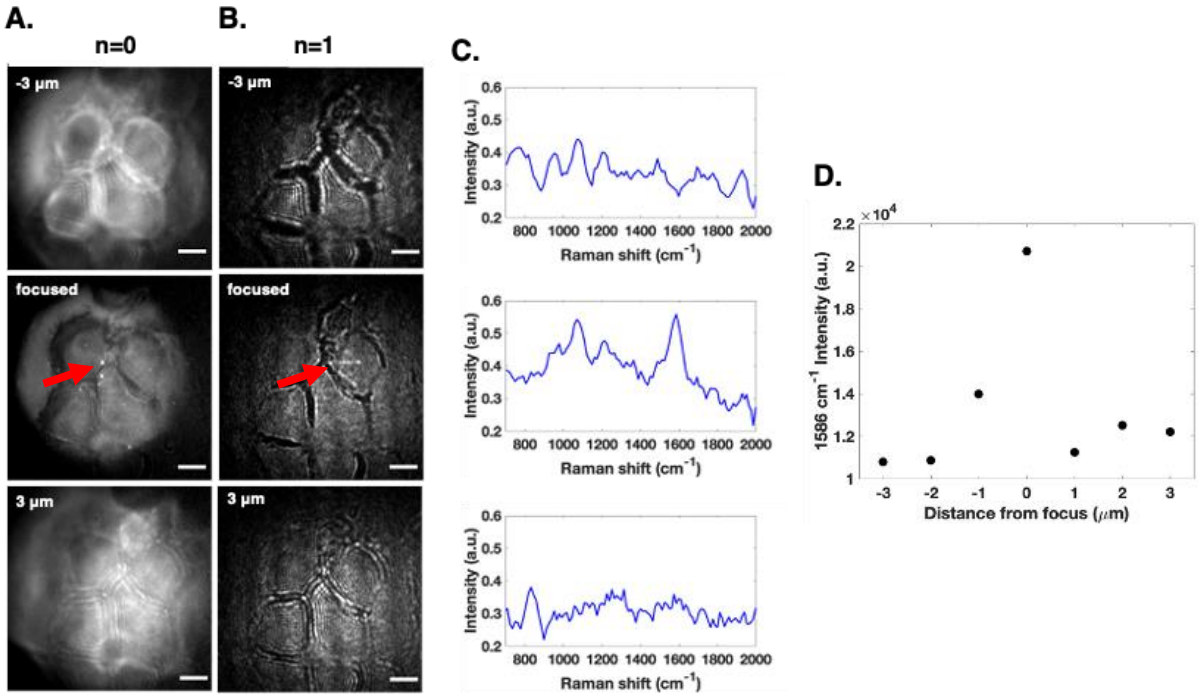

Figure 5. A) Cropped images of the SERS scattering and bright field of AuNP@Silica in fixed cells in the n=0 region and (B) average SERS scattering of AuNP@Silica in fixed cells in the n=1 region of the CMOS sensor at the specified focal planes: -3 µm (top), 0 µm (center), 3 µm (bottom) offset in the z-direction. Scale bars are 5 µm. C) SERS spectra of AuNP@Silica particles from the images in (B). D) Plot of intensities of the 1586 cm^{-1} MBA band as a function of focal plane.

We extended our approach to image MBA functionalized AuNP@Silica particles in fixed human colon cancer cells to show nanoparticles can be detected in the cells while simultaneously obtaining images and spectra at various focal planes. The cells have a 10 µm diameter which enabled multiple cells to be illuminated with the laser. Bright field images of the cells without laser illumination are shown in Figure S5. Figure 5A shows bright filed images of the n=0 order of the cells illuminated by a white light and the laser to show cellular features and the AuNP@Silica particles. The FWHM of the AuNP@Silica particle in the focused image is 356 nm, which is localized to 65 nm in the super-resolution result. Images were acquired with the cells and

nanoparticles in focus and 3 μm in either direction in the z-plane. Figure 5B shows the n=1 order of the same cells illuminated by only the laser. The nanoparticle and its spectral response chosen for analysis are indicated by the red arrows in Figure 5A and B. The spectral response from the nanoparticle is present in the n=1 order, but there is also residual Rayleigh scattering from the cellular membranes present. To show this, we analyzed the same region in both the n=0 and n=1 orders (Figure S6), showing that many of features in the n=1 order are also present in the n=0 order. Therefore, these features are not indicative of SERS but rather Rayleigh scattering that passed through the longpass filter. It is worth noting that both Raman and Rayleigh scattering contribute to the signal in the n=0 order, but the magnitude of intensity in the n=1 compared to the n=0 (Figure S6) suggests that the Raman scattering is more intense than the Rayleigh scattering. A difference/sum ratio was applied to the n=0 and n=1 spectra shown in Figure S6 for the 3 chosen focal planes, and the resulting spectra are shown in Figure 5C. The spectrum from the focal plane where the nanoparticle is in focus (Figure 5C, center spectrum) shows MBA peaks at 1070 cm^{-1} and 1586 cm^{-1} that are not present when the focal plane is offset by 3 μm in the z-plane (Figure 5C, top and bottom spectra). Figure 5D shows the intensity of the 1586 cm^{-1} band as a function of focal depth from the depth where the nanoparticle is in focus. The 1586 cm^{-1} band is most intense when the particle is in focus and decreases as the focal depth is offset, further demonstrating the sensitivity of the spectral response for optical sectioning of the nanoparticles in 3D.

Discussion

Our results show the capability to directly correlate spectra to spatial features by using a wide-field imaging approach that simultaneously captures both spatial and spectral information on a single sCMOS sensor. Nanoparticles are ideal materials to image with this approach and make it particularly appropriate for SERS imaging due to the Raman signal enhancement that arises from the plasmonic nanoparticles. In comparison to spontaneous Raman, where the sample homogeneity would dramatically limit spectral resolution, similar to the large pinholes used in Figure 3, the plasmonic nanoparticle provide point sources, diffraction limited virtual slits, for generating the SERS spectra in the n=1 portion of the image.

A significant tradeoff of this technique is the spectral resolution compared to that obtained from using a traditional Raman spectrometer. This is in part due to using a 300 groove/mm diffraction grating as the diffraction element, but incorporating a grating with a greater groove

density would not enable both the n=0 and n=1 order to be captured on the same sensor at the same grating to sensor distance and would increase the likelihood of spectral overlap from neighboring particles. However, optimization of instrument parameters with respect to the size of the sCMOS sensor successfully enables simultaneous imaging and spectroscopy with ~13 cm^{-1}/pixel resolution in the spectral domain.

A key advantage to this approach is that SIFs are readily captured which enables the application of super resolution and localization algorithms, specifically STORM. Prior reports have taken advantage of a SERS wide field imaging approach and SIFs to obtain super resolution images with sub diffraction limited resolution without the need for a fluorescent molecule, but a separate spectrometer was required to provide SERS spectra.[36, 39, 59, 60] Lindquist et al. used a similar spectrally resolved SERS imaging approach to spectrally differentiate between gram positive and gram negative bacteria and applied STORM fittings to super resolve the spatial domain.[38] In this study, we demonstrate that applying the STORM fitting to the image stack containing both the n=0 and n=1 orders not only localizes the PSF of the image in the n=0 order, but also the spectral response in the n=1 order. This provides improved peak identification by localizing the bands in the spectral regime to one pixel on the sensor and removes the non-fluctuating background that is present in the raw image stack. In addition, applying the STORM fitting to the n=1 identifies frequency fluctuating components that are otherwise lost by spectral integration. This improved peak identification requires the spectrum to be acquired simultaneously, which is not possible using an LCTF for wide-field SERS imaging. Our group has previously demonstrated with spectrally resolved SERS imaging that these frequency fluctuations are consistent with density functional theory (DFT) calculations of MBA anion and cation radical species.[44] Here, the STORM fitting of the n=1 domain (shown in Figure 4D) identifies bands at 1276 and 1513 cm^{-1} that are consistent with bands observed in the DFT calculated MBA anion radical SERS spectrum.[44]

We also demonstrate a new method to correlate SERS imaging to spectra in 3D by using the spectrally resolved SERS imaging approach to detect and image SERS labelled nanoparticles on fixed cells. Our results show the ability to image nanoparticles in cells while simultaneously detecting SERS labels on a much faster timescale than confocal Raman cell mapping and illustrate the potential to investigate interactions inside of cells with super resolution SERS. Previous studies have used TERS to image cells with nanoscale resolution and simultaneous Raman spectral

analysis to probe cellular surfaces and understand biomolecular interactions.[61-63] However, TERS has limited penetration depth and studies using TERS to investigate cellular systems have been limited to surface interactions [64, 65] or require cell sectioning to observe intracellular interactions.[66] The imaging approach described herein demonstrates the sensitivity of the SERS response to the focal plane and the promising potential for further studies to study nanoparticle interactions inside cells with super resolution SERS. A challenge in using this approach to image nanoparticles on cells is the background scattering present in the images. It is well known that features larger than the excitation wavelength have dominant forward scattering.[67] In our study, this makes the scattering from cellular boundaries more evident while spontaneous Raman scattering from these structures is not resolved. In contrast, the nanoparticles show increased uniform scattering with Raman scattering that becomes intense and resolvable in the appropriate focal plane. The Rayleigh and Raman scattering from the particles is significantly stronger than the background scattering from the cellular environment. Further development will differentiate the nanoparticle scattering from cellular features to reduce the background that appears in the spectral region.

Conclusions

In conclusion, we describe a wide field SERS imaging technique capable of directly correlating image features to Raman spectra by using a diffraction grating prior to the sensor to separate the image plane into a spatial and spectral domain. By acquiring on the 100 millisecond timescale, our system can readily observe SIFs and frequency fluctuations from the spectral response of many particles in the FOV. Applying STORM algorithms enables super-resolution imaging simultaneously with spectrum acquisition and also successfully provides improved peak identification consistent with features in the observed signal fluctuations. In the present work, we used the improved peak localization to identify fluctuating components consistent with prior DFT calculations of radical MBA species. We also demonstrate the application of this technique to detect SERS labels in fixed cells and show the sensitivity of the spectral response dependent on focal plane, illustrating the capability to probe particles in 3D and possibly improve z-localization. This approach has potential to be used in a variety of biological and physical applications where correlating the spatial origin of the Raman signal to chemical interactions originating from interactions with surrounding environment is beneficial.

ASSOCIATED CONTENT

Supporting Information

The Supporting Information is available free of charge on the ACS Publications website.

Supplementary figures S1-S6 and Table S1 provide characterization of the field of view, calculated dispersion, nanoparticle characterization, bright field cell images, and additional spectroscopic results.

AUTHOR INFORMATION

Corresponding Author

* Corresponding author email: Schultz.133@osu.edu

Author Contributions

DNS performed all imaging experiments and instrument development. BTS synthesized and functionalized the nanoparticles used. DNS and ZDS analyzed the results. ZDS conceptualized the experiment, supervised the research, and obtained funding for the study. DNS prepared the manuscript with contributions from all the authors. All authors have given approval to the final version of the manuscript.

ACKNOWLEDGMENT

Electron microscopy was performed at the Center for Electron Microscopy and Analysis (CEMAS) at The Ohio State University. The research reported here was supported by Awards from the National Institutes of Health, National Institute for General Medical Sciences award R01 GM109988, through the Ohio State Comprehensive Cancer Center support from the National Cancer Institute P30 CA016058, and the National Science Foundation Award CHE-2107791.

References

1. Xiao, L.; Schultz, Z. D., Spectroscopic Imaging at the Nanoscale: Technologies and Recent Applications. *Analytical Chemistry* **2018,** *90* (1), 440-458.

2. Antonio, K. A.; Schultz, Z. D., Advances in Biomedical Raman Microscopy. *Analytical Chemistry* **2014,** *86* (1), 30-46.

3. Dong, X.; Jakobi, M.; Wang, S.; Köhler, M. H.; Zhang, X.; Koch, A. W., A review of hyperspectral imaging for nanoscale materials research. *Applied Spectroscopy Reviews* **2019,** *54* (4), 285-305.

4. Klenerman, D.; Korchev, Y.; Novak, P.; Shevchuk, A., Noncontact Nanoscale Imaging of Cells. *Annual Review of Analytical Chemistry* **2021,** *14*, 347-361.

5. Moerner, W. E.; Kador, L., Optical detection and spectroscopy of single molecules in a solid. *Physical review letters* **1989,** *62* (21), 2535.

6. Betzig, E., Proposed method for molecular optical imaging. *Optics letters* **1995,** *20* (3), 237-239.

7. Betzig, E.; Patterson, G. H.; Sougrat, R.; Lindwasser, O. W.; Olenych, S.; Bonifacino, J. S.; Davidson, M. W.; Lippincott-Schwartz, J.; Hess, H. F., Imaging intracellular fluorescent proteins at nanometer resolution. *science* **2006,** *313* (5793), 1642-1645.

8. Hell, S. W.; Wichmann, J., Breaking the diffraction resolution limit by stimulated emission: stimulated-emission-depletion fluorescence microscopy. *Optics letters* **1994,** *19* (11), 780-782.

9. Klar, T. A.; Jakobs, S.; Dyba, M.; Egner, A.; Hell, S. W., Fluorescence microscopy with diffraction resolution barrier broken by stimulated emission. *Proceedings of the National Academy of Sciences* **2000,** *97* (15), 8206-8210.

10. Hell, S. W.; Kroug, M., Ground-state-depletion fluorscence microscopy: A concept for breaking the diffraction resolution limit. *Applied Physics B* **1995,** *60* (5), 495-497.

11. Schlücker, S.; Schaeberle, M. D.; Huffman, S. W.; Levin, I. W., Raman microspectroscopy: a comparison of point, line, and wide-field imaging methodologies. *Analytical Chemistry* **2003,** *75* (16), 4312-4318.

12. Bhargava, R.; Levin, I. W., Time-resolved Fourier transform infrared spectroscopic imaging. *Applied spectroscopy* **2003,** *57* (4), 357-366.

13. Abraham, J. L.; Etz, E. S., Molecular microanalysis of pathological specimens in situ with a laser-Raman microprobe. *Science* **1979,** *206* (4419), 716-718.

14. Stewart, S.; Priore, R. J.; Nelson, M. P.; Treado, P. J., Raman imaging. *Annual Review of Analytical Chemistry* **2012,** *5*, 337-360.

15. Lewis, E. N.; Treado, P. J.; Reeder, R. C.; Story, G. M.; Dowrey, A. E.; Marcott, C.; Levin, I. W., Fourier transform spectroscopic imaging using an infrared focal-plane array detector. *Analytical chemistry* **1995,** *67* (19), 3377-3381.

16. Kong, L.; Zhang, P.; Yu, J.; Setlow, P.; Li, Y.-q., Rapid confocal Raman imaging using a synchro multifoci-scan scheme for dynamic monitoring of single living cells. *Applied Physics Letters* **2011,** *98* (21), 213703.

17. Krafft, C.; Schmitt, M.; Schie, I. W.; Cialla-May, D.; Matthäus, C.; Bocklitz, T.; Popp, J., Label-free molecular imaging of biological cells and tissues by linear and nonlinear Raman spectroscopic approaches. *Angewandte Chemie International Edition* **2017,** *56* (16), 4392-4430.

18. Gong, L.; Zheng, W.; Ma, Y.; Huang, Z., Higher-order coherent anti-Stokes Raman scattering microscopy realizes label-free super-resolution vibrational imaging. *Nature Photonics* **2020,** *14* (2), 115-122.

19. Cheng, J.-X.; Xie, X. S., Vibrational spectroscopic imaging of living systems: An emerging platform for biology and medicine. *Science* **2015,** *350* (6264), aaa8870.

20. Fleischmann, M.; Hendra, P. J.; McQuillan, A. J., Raman spectra of pyridine adsorbed at a silver electrode. *Chemical physics letters* **1974,** *26* (2), 163-166.

21. Jeanmaire, D. L.; Van Duyne, R. P., Surface Raman spectroelectrochemistry: Part I. Heterocyclic, aromatic, and aliphatic amines adsorbed on the anodized silver electrode. *Journal of electroanalytical chemistry and interfacial electrochemistry* **1977,** *84* (1), 1-20.

22. Moskovits, M., Surface roughness and the enhanced intensity of Raman scattering by molecules adsorbed on metals. *The Journal of Chemical Physics* **1978,** *69* (9), 4159-4161.

23. Langer, J.; Jimenez de Aberasturi, D.; Aizpurua, J.; Alvarez-Puebla, R. A.; Auguié, B.; Baumberg, J. J.; Bazan, G. C.; Bell, S. E.; Boisen, A.; Brolo, A. G., Present and future of surface-enhanced Raman scattering. *ACS nano* **2019,** *14* (1), 28-117.

24. Nie, S.; Emory, S. R., Probing single molecules and single nanoparticles by surface-enhanced Raman scattering. *science* **1997,** *275* (5303), 1102-1106.

25. Kneipp, K.; Wang, Y.; Kneipp, H.; Perelman, L. T.; Itzkan, I.; Dasari, R. R.; Feld, M. S., Single molecule detection using surface-enhanced Raman scattering (SERS). *Physical review letters* **1997,** *78* (9), 1667.

26. Fabris, L., SERS tags: the next promising tool for personalized cancer detection? *ChemNanoMat* **2016,** *2* (4), 249-258.

27. Goodacre, R.; Graham, D.; Faulds, K., Recent developments in quantitative SERS: Moving towards absolute quantification. *TrAC Trends in Analytical Chemistry* **2018,** *102*, 359-368.

28. Vo-Dinh, T.; Liu, Y.; Fales, A. M.; Ngo, H.; Wang, H. N.; Register, J. K.; Yuan, H.; Norton, S. J.; Griffin, G. D., SERS nanosensors and nanoreporters: golden opportunities in biomedical applications. *Wiley Interdisciplinary Reviews: Nanomedicine and Nanobiotechnology* **2015,** *7* (1), 17-33.

29. Nguyen, A. H.; Peters, E. A.; Schultz, Z. D., Bioanalytical applications of surface-enhanced Raman spectroscopy: de novo molecular identification. *Reviews in Analytical Chemistry* **2017,** *36* (4), 20160037.

30. Asiala, S. M.; Schultz, Z. D., Label-free in situ detection of individual macromolecular assemblies by surface enhanced Raman scattering. *Chemical Communications* **2013,** *49* (39), 4340-4342.

31. Scott, B.; Carron, K., Dynamic surface enhanced Raman spectroscopy (SERS): extracting SERS from normal Raman scattering. *Analytical chemistry* **2012,** *84* (20), 8448-8451.

32. dos Santos, D. P.; Temperini, M. L. A.; Brolo, A. G., Intensity Fluctuations in Single-Molecule Surface-Enhanced Raman Scattering. *Accounts of Chemical Research* **2019,** *52* (2), 456-464.

33. Willets, K. A.; Wilson, A. J.; Sundaresan, V.; Joshi, P. B., Super-resolution imaging and plasmonics. *Chemical reviews* **2017,** *117* (11), 7538-7582.

34. Rust, M. J.; Bates, M.; Zhuang, X., Sub-diffraction-limit imaging by stochastic optical reconstruction microscopy (STORM). *Nature methods* **2006,** *3* (10), 793-796.

35. Titus, E. J.; Weber, M. L.; Stranahan, S. M.; Willets, K. A., Super-resolution SERS imaging beyond the single-molecule limit: an isotope-edited approach. *Nano letters* **2012,** *12* (10), 5103-5110.

36. Stranahan, S. M.; Willets, K. A., Super-resolution Optical Imaging of Single-Molecule SERS Hot Spots. *Nano Letters* **2010,** *10* (9), 3777-3784.

37. Lindquist, N. C.; de Albuquerque, C. D. L.; Sobral-Filho, R. G.; Paci, I.; Brolo, A. G., High-speed imaging of surface-enhanced Raman scattering fluctuations from individual nanoparticles. *Nature nanotechnology* **2019,** *14* (10), 981-987.

38. Olson, A. P.; Spies, K. B.; Browning, A. C.; Soneral, P. A.; Lindquist, N. C., Chemically imaging bacteria with super-resolution SERS on ultra-thin silver substrates. *Scientific reports* **2017,** *7* (1), 1-9.
39. de Albuquerque, C. D. L.; Schultz, Z. D., Super-resolution surface-enhanced Raman scattering imaging of single particles in cells. *Analytical Chemistry* **2020,** *92* (13), 9389-9398.
40. Wang, L.; Dai, Y.; He, H.; Lv, R.; Zong, C.; Ren, B., Dynamic Raman imaging system with high spatial and temporal resolution. *Review of Scientific Instruments* **2017,** *88* (9), 095110.
41. Bongiovanni, M. N.; Godet, J.; Horrocks, M. H.; Tosatto, L.; Carr, A. R.; Wirthensohn, D. C.; Ranasinghe, R. T.; Lee, J.-E.; Ponjavic, A.; Fritz, J. V., Multi-dimensional super-resolution imaging enables surface hydrophobicity mapping. *Nature communications* **2016,** *7* (1), 1-9.
42. Al-Zubeidi, A.; Hoener, B. S.; Collins, S. S.; Wang, W.; Kirchner, S. R.; Hosseini Jebeli, S. A.; Joplin, A.; Chang, W.-S.; Link, S.; Landes, C. F., Hot holes assist plasmonic nanoelectrode dissolution. *Nano Letters* **2019,** *19* (2), 1301-1306.
43. Heider, E. C.; Barhoum, M.; Peterson, E. M.; Schaefer, J.; Harris, J. M., Identification of single fluorescent labels using spectroscopic microscopy. *Applied spectroscopy* **2010,** *64* (1), 37-45.
44. de Albuquerque, C. D. L.; Zoltowski, C. M.; Scarpitti, B. T.; Shoup, D. N.; Schultz, Z. D., Spectrally Resolved Surface-Enhanced Raman Scattering Imaging Reveals Plasmon-Mediated Chemical Transformations. *ACS Nanoscience Au* **2021,** *1* (1), 38-46.
45. Zhang, R.; Zhang, Y.; Dong, Z.; Jiang, S.; Zhang, C.; Chen, L.; Zhang, L.; Liao, Y.; Aizpurua, J.; Luo, Y. e., Chemical mapping of a single molecule by plasmon-enhanced Raman scattering. *Nature* **2013,** *498* (7452), 82-86.
46. Lee, J.; Crampton, K. T.; Tallarida, N.; Apkarian, V., Visualizing vibrational normal modes of a single molecule with atomically confined light. *Nature* **2019,** *568* (7750), 78-82.
47. Frens, G., Controlled nucleation for the regulation of the particle size in monodisperse gold suspensions. *Nature physical science* **1973,** *241* (105), 20-22.
48. Yao, T.; Asayama, Y., Animal-cell culture media: History, characteristics, and current issues. *Reproductive medicine and biology* **2017,** *16* (2), 99-117.

49. Ovesný, M.; Křížek, P.; Borkovec, J.; Švindrych, Z.; Hagen, G. M., ThunderSTORM: a comprehensive ImageJ plug-in for PALM and STORM data analysis and super-resolution imaging. *Bioinformatics* **2014,** *30* (16), 2389-2390.

50. de Albuquerque, C. D. L.; Hokanson, K. M.; Thorud, S. R.; Sobral-Filho, R. G.; Lindquist, N. C.; Brolo, A. G., Dynamic imaging of multiple SERS hotspots on single nanoparticles. *ACS Photonics* **2020,** *7* (2), 434-443.

51. Willets, K. A., Super-resolution imaging of SERS hot spots. *Chemical Society Reviews* **2014,** *43* (11), 3854-3864.

52. Mazaheri, L.; Jelken, J.; Avilés, M. O.; Legge, S.; Lagugné-Labarthet, F., Investigating the Performances of Wide-Field Raman Microscopy with Stochastic Optical Reconstruction Post-Processing. *Applied Spectroscopy* **2022**, 00037028211056975.

53. Wilson, A. J.; Willets, K. A., Visualizing site-specific redox potentials on the surface of plasmonic nanoparticle aggregates with superlocalization SERS microscopy. *Nano letters* **2014,** *14* (2), 939-945.

54. Wu, Y.; Yang, M.; Ueltschi, T. W.; Mosquera, M. A.; Chen, Z.; Schatz, G. C.; Van Duyne, R. P., SERS study of the mechanism of plasmon-driven hot electron transfer between gold nanoparticles and PCBM. *The Journal of Physical Chemistry C* **2019,** *123* (49), 29908-29915.

55. Szczerbiński, J.; Gyr, L.; Kaeslin, J.; Zenobi, R., Plasmon-Driven Photocatalysis Leads to Products Known from E-beam and X-ray-Induced Surface Chemistry. *Nano Letters* **2018,** *18* (11), 6740-6749.

56. Choi, H.-K.; Lee, K. S.; Shin, H.-H.; Kim, Z. H., Identification of the First Elementary Step in the Photocatalytic Reduction of Nitrobenzenethiols on a Metallic Surface. *The Journal of Physical Chemistry Letters* **2016,** *7* (20), 4099-4104.

57. Sprague-Klein, E. A.; McAnally, M. O.; Zhdanov, D. V.; Zrimsek, A. B.; Apkarian, V. A.; Seideman, T.; Schatz, G. C.; Van Duyne, R. P., Observation of Single Molecule Plasmon-Driven Electron Transfer in Isotopically Edited 4,4′-Bipyridine Gold Nanosphere Oligomers. *Journal of the American Chemical Society* **2017,** *139* (42), 15212-15221.

58. Michota, A.; Bukowska, J., Surface-enhanced Raman scattering (SERS) of 4-mercaptobenzoic acid on silver and gold substrates. *Journal of Raman Spectroscopy* **2003,** *34* (1), 21-25.

59. Liang, L.; Zheng, P.; Zhang, C.; Barman, I., A Programmable DNA-Silicification-Based Nanocavity for Single-Molecule Plasmonic Sensing. *Advanced Materials* **2021,** *33* (7), 2005133.
60. Weber, M. L.; Willets, K. A., Correlated Super-Resolution Optical and Structural Studies of Surface-Enhanced Raman Scattering Hot Spots in Silver Colloid Aggregates. *The Journal of Physical Chemistry Letters* **2011,** *2* (14), 1766-1770.
61. Alexander, K. D.; Schultz, Z. D., Tip-Enhanced Raman Detection of Antibody Conjugated Nanoparticles on Cellular Membranes. *Analytical Chemistry* **2012,** *84* (17), 7408-7414.
62. Neugebauer, U.; Rösch, P.; Schmitt, M.; Popp, J.; Julien, C.; Rasmussen, A.; Budich, C.; Deckert, V., On the way to nanometer-sized information of the bacterial surface by tip-enhanced Raman spectroscopy. *Chemphyschem: a European journal of chemical physics and physical chemistry* **2006,** *7* (7), 1428-1430.
63. Xiao, L.; Bailey, K. A.; Wang, H.; Schultz, Z. D., Probing Membrane Receptor–Ligand Specificity with Surface- and Tip- Enhanced Raman Scattering. *Analytical Chemistry* **2017,** *89* (17), 9091-9099.
64. Vitol, E. A.; Orynbayeva, Z.; Friedman, G.; Gogotsi, Y., Nanoprobes for intracellular and single cell surface-enhanced Raman spectroscopy (SERS). *Journal of Raman Spectroscopy* **2012,** *43* (7), 817-827.
65. Deckert-Gaudig, T.; Taguchi, A.; Kawata, S.; Deckert, V., Tip-enhanced Raman spectroscopy–from early developments to recent advances. *Chemical Society Reviews* **2017,** *46* (13), 4077-4110.
66. Wood, B. R.; Bailo, E.; Khiavi, M. A.; Tilley, L.; Deed, S.; Deckert-Gaudig, T.; McNaughton, D.; Deckert, V., Tip-enhanced Raman scattering (TERS) from hemozoin crystals within a sectioned erythrocyte. *Nano letters* **2011,** *11* (5), 1868-1873.
67. Bohren, C. F.; Huffman, D. R., *Absorption and scattering of light by small particles*. John Wiley & Sons: 2008.

TOC Graphic

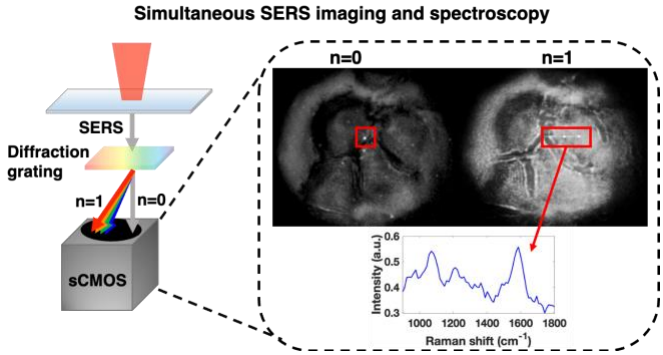
Simultaneous SERS imaging and spectroscopy
SERS
Diffraction grating
n=1
n=0
sCMOS
n=0
n=1
Intensity (a.u.)
0.6
0.5
0.4
0.3
1000
1200
1400
1600
1800
Raman shift (cm-1)